ACS APPLIED MATERIALS & INTERFACES

Research Article

www.acsami.org

One-Step Hydrothermal Synthesis of 3D Petal-like Co_9S_8/RGO/Ni_3S_2 Composite on Nickel Foam for High-Performance Supercapacitors

Zhuomin Zhang, Qian Wang, Chongjun Zhao,* Shudi Min, and Xiuzhen Qian

Key Laboratory for Ultrafine Materials of Ministry of Education, School of Materials Science and Engineering, East China University of Science and Technology, Meilong Road 130, Shanghai 200237, P.R. China

Supporting Information

ABSTRACT: Co_9S_8, Ni_3S_2, and reduced graphene oxide (RGO) were combined to construct a graphene composite with two mixed metal sulfide components. Co_9S_8/RGO/Ni_3S_2 composite films were hydrothermal-assisted synthesized on nickel foam (NF) by using a modified "active metal substrate" route in which nickel foam acted as both a substrate and Ni source for composite films. It is found that the Co_9S_8/RGO/Ni_3S_2/NF electrode exhibits superior capacitive performance with high capability (13.53 F cm^{-2} at 20 mA cm^{-2}, i.e., 2611.9 F g^{-1} at 3.9 A g^{-1}), excellent rate capability, and enhanced electrochemical stability, with 91.7% retention after 1000 continuous charge−discharge cycles even at a high current density of 80 mA cm^{-2}.

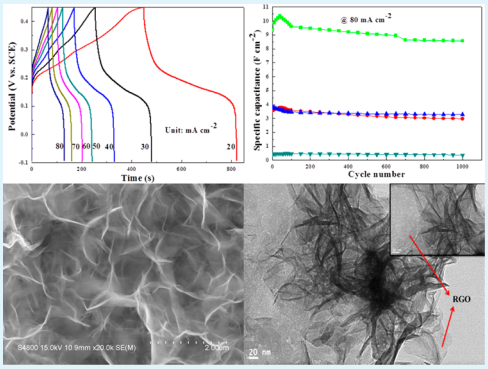

KEYWORDS: *Co_9S_8/RGO/Ni_3S_2 composites, supercapacitor, Ni foam, hydrothermal method, chemical redox*

1. INTRODUCTION

Electrochemical capacitors (supercapacitors) have attracted increasing attention because of their higher energy density than common dielectric capacitors and higher power density than secondary batteries.[1,2] Moreover, they are considered as encouraging power supplier and energy storage devices, which require fast charge−discharge rates and long cycle life.[2−4]

Supercapacitors are generally classified into two categories: electrical double layer capacitors (EDLC) and pseudocapacitors, according to the electrode materials (i.e., storage mechanism) used, of which pseudocapacitors are expected to overcome the disadvantage of low energy density in EDLC supercapacitors.[5,6]

Obviously, not only the kind of supercapacitors but also their performances strongly depend on the intrinsic properties of the active materials of supercapacitors. Both transition metal oxides and conducting polymers have been widely investigated and chosen as active materials of pseudocapacitors. Presently, due to excellent chemical stability, rich valences,[7−9] and good electrochemical performance, various transition metal sulfides have also been candidates in this field.[7,8,10−13] Among these transition metal sulfides, both Ni_3S_2 and Co_9S_8 exhibited good electrochemical performance and therefore have attracted substantially more attention.[12,13]

To enhance the capability of these active materials of Ni_3S_2 and Co_9S_8, these transition metal sulfides were synthesized in terms of morphology and structure so as to further improve their performance.[13−15] It is found that nanosized and porous structures facilitate their capacities.[16]

On the other hand, because of synergistic effects, compositing is an alternative method to efficiently enhance the performance of single-component active materials. First, compositing with graphene is considered to be a viable way. Owing to its unique merits including high electronic conductivity (16000 S/m)[17] and high specific surface area (2630 m^2/g, theoretical value),[18] graphene in composites acts as a soft support for the deposition of active nanoparticles and a second current collector for electron transfer at the nanoscale. Furthermore, flexible graphene also serves as a buffer to alleviate possible volume changes during charge/discharge process, especially in cyclability test processes.[19] Up to now, this compositing method has been utilized successfully.[19−21] Second, ternary transition metal sulfides, e.g., $NiCo_2S_4$, can supply richer redox processes than the single component sulfides.[3−5] Especially, this method can be used as a bind-free electrode preparation to deposit the active materials of $NiCo_2S_4$ on the conductive substrates of carbon fiber paper and nickel foam.[4,5,22] Third, Wei et al. developed a bind-free and direct growth method of active materials on NF and prepared a composite of Ni_3S_2 and Co_9S_8 (Ni_3S_2@Co_9S_8) through a two-step route of partial ion-exchange of nickel sulfide of nest-like Ni_3S_2@NiS.[3] As Ni foam acted as a template, Ni source, and substrate (current collector), a direct way to grow Ni_3S_2/Co_9S_8 composite film (electrode) can be achieved without the addition of extra salts as an Ni source and bind-free based on

Received: December 14, 2014
Accepted: February 17, 2015
Published: February 17, 2015

DOI: 10.1021/am5088192
ACS Appl. Mater. Interfaces 2015, 7, 4861−4868

the in situ redox reaction of Ni and sulfur during the hydrothermal process.[23] This indicates that the electrode preparation process, including careful grinding and coating procedures which are necessary for powdery active materials, becomes unnecessary.[24,25]

Despite these advancements, to the best of our knowledge, there is no report on the direct preparation of a composite of Co_9S_8/RGO/Ni_3S_2 on NF through a one-step route without the addition of Ni salts, in which NF acts as both a substrate and Ni source.

In this work, we report a simple hydrothermal route to prepare Co_9S_8/RGO/Ni_3S_2 on Ni foam by using nickel foam as both a substrate and Ni ion source of Ni_3S_2. On the basis of the redox reaction of elemental Ni and GO[26] and further conversion into Ni_3S_2/RGO composite[19] during a hydrothermal process, as well as the transformation of Co^{2+} into Co_9S_8 and subsequent deposition on NF through a hydrothermal method at a similar temperature (160 °C for Co_9S_8 vs 180 °C for Ni_3S_2),[27] a composite of Ni_3S_2, Co_9S_8, and RGO was synthesized through a one-step hydrothermal process. As-prepared Co_9S_8/RGO/Ni_3S_2 (CRNS) was directly used as a supercapacitor electrode and exhibited superior supercapacitor performance, e.g., 13.53 F cm^{-2} at 20 mA cm^{-2} (i.e., 2611.9 F g^{-1} at 3.9 A g^{-1}), compared with the Co_9S_8/Ni_3S_2 (CNS) electrode (7.02 F cm^{-2} at 20 mA cm^{-2}) and the RGO/Ni_3S_2 (RNS) electrode (7.77 F cm^{-2} at 20 mA cm^{-2}) prepared under identical conditions.

2. EXPERIMENTAL SECTION

2.1. Synthesis of Co_9S_8/RGO/Ni_3S_2, Co_9S_8/Ni_3S_2, and RGO/Ni_3S_2 Composites on NF. Graphene oxide (GO) was prepared by the chemical oxidation method.[26,28] The cleaned NF (1 × 2 cm^2) with a bared area of 1 × 1 cm^2 was then immersed in the aqueous solution of GO (25 mg), cobalt salt (1 mmol), and thiourea (2 mmol). The hydrothermal synthesis of Co_9S_8/RGO/Ni_3S_2 composites was carried out at some different temperatures (i.e., 150, 180, 210, and 240 °C) for 24 h. The obtained Co_9S_8/RGO/Ni_3S_2 was flushed with water and ethanol in turn and then dried at 80 °C for 10 h. Co_9S_8/RGO/Ni_3S_2/NF composites were denoted as CRNS-150, CRNS-180, CRNS-210, and CRNS-240 according to the hydrothermal treatment temperatures. For comparison, Co_9S_8/Ni_3S_2/NF (CNS-180), RGO/Ni_3S_2/NF (RNS-180), and Ni_3S_2/NF (NS-180) composites were prepared under identical conditions (180 °C, 24 h).

2.2. Characterizations of Co_9S_8/RGO/Ni_3S_2 Composites. XRD was carried out on an X-ray diffractionmeter with Cu Kα (λ = 0.15406 nm). Raman spectra were performed by using an INVIA Raman microprobe (laser wavelength: 514 nm). XPS spectra were tested on an ESCALAB 250Xi (Thermo Fisher) instrument. The morphology and structure of composites were monitored by using FESEM (Hitachi S-4800) and TEM (JEOL JEM-2100), respectively.

2.3. Electrochemical Testing. The electrochemical performances of Co_9S_8/RGO/Ni_3S_2 composite were carried out on the electrochemical workstation of CHI 660e, in which Co_9S_8/RGO/Ni_3S_2, Pt foil, and SCE acted as working electrode, counter electrode, and reference electrode, respectively. An aqueous solution of 2 M KOH was served as the electrolyte. The loading amount of Co_9S_8/RGO/Ni_3S_2 electrode was defined according to the method reported in previous work.[19,26] Supporting Information Figures S1 and S2 show the images of FESEM, CV, and GCD of virgin NF and NF substrate after the Co_9S_8/RGO/Ni_3S_2 was peeled off by ultrasonic treatment.

3. RESULTS AND DISCUSSION

3.1. Characterization of Co_9S_8/RGO/Ni_3S_2 Composites. X-ray diffraction (XRD) patterns of Co_9S_8/RGO/Ni_3S_2/NF (CRNS), Co_9S_8/Ni_3S_2/NF (CNS), and RGO/Ni_3S_2/NF (RNS) composites prepared at 180 °C are shown in Figure 1.

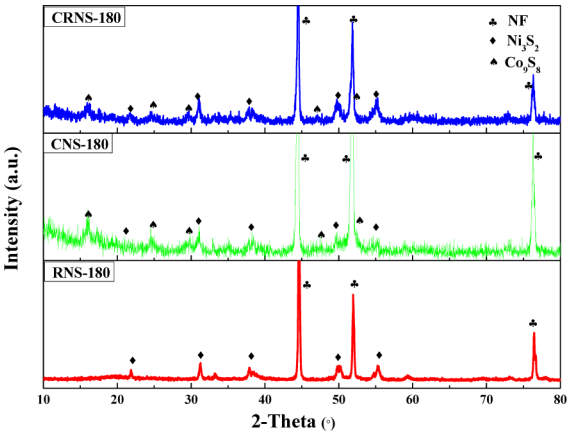

Figure 1. XRD patterns of CRNS-180, CNS-180, and RNS-180.

Three peaks centered at 44.6°, 51.9°, and 76.4° which are assigned to the (111), (200), and (220) planes of metallic nickel (JCPDS no. 01-1258),[12] respectively, are distinctly found in the XRD patterns of all composite samples. For RNS-180 composite, five peaks emerge at 21.7°, 31.1°, 37.7°, 50.1°and 55.3°, which correspond to (101), (110), (003), (211) and (300) of Ni_3S_2 (JCPDS no. 44-1418), respectively.[12] Referring to CRNS-180 and CNS-180, besides those peaks of Ni_3S_2, another five peaks are observed at 15.4°, 25.1°, 29.8°, 47.5°, and 52.1°, which belong to Co_9S_8 (JCPDS no. 65-1765).[27] Therefore, it is reasonable to conclude that both Ni_3S_2 and Co_9S_8 have been fabricated, i.e., Ni foam was decorated with the Ni_3S_2 and Co_9S_8.

Although the peak of RGO in the Co_9S_8/RGO/Ni_3S_2 composite is not obviously observed in the XRD patterns above, its presence of RGO is verified by Raman results shown in Figure 2.

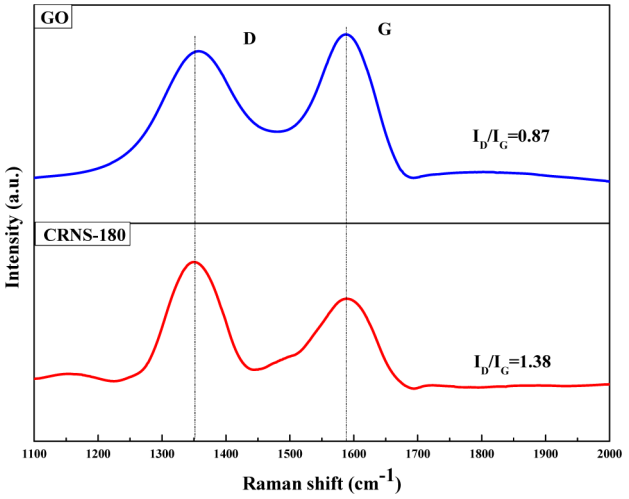

Figure 2. Raman spectra of CRNS-180 and GO.

Two distinct peaks occur at 1352 cm^{-1} (D band) and 1588 cm^{-1} (G band) for CRNS-180, matching with the breathing mode of A_{1g} symmetry and the E_{2g} mode of sp^2-bonded carbon atoms, respectively, suggesting the existence of RGO. The ratio of the G band (~1588 cm^{-1}) and the D band (~1352 cm^{-1}) is applied to semiquantitatively identify the reduction extent.[26,29] Compared with GO (0.87), RGO has a higher D/G ratio (1.38), i.e., average size of the sp^2 domains decrease. This

DOI: 10.1021/am5088192
ACS Appl. Mater. Interfaces 2015, 7, 4861−4868

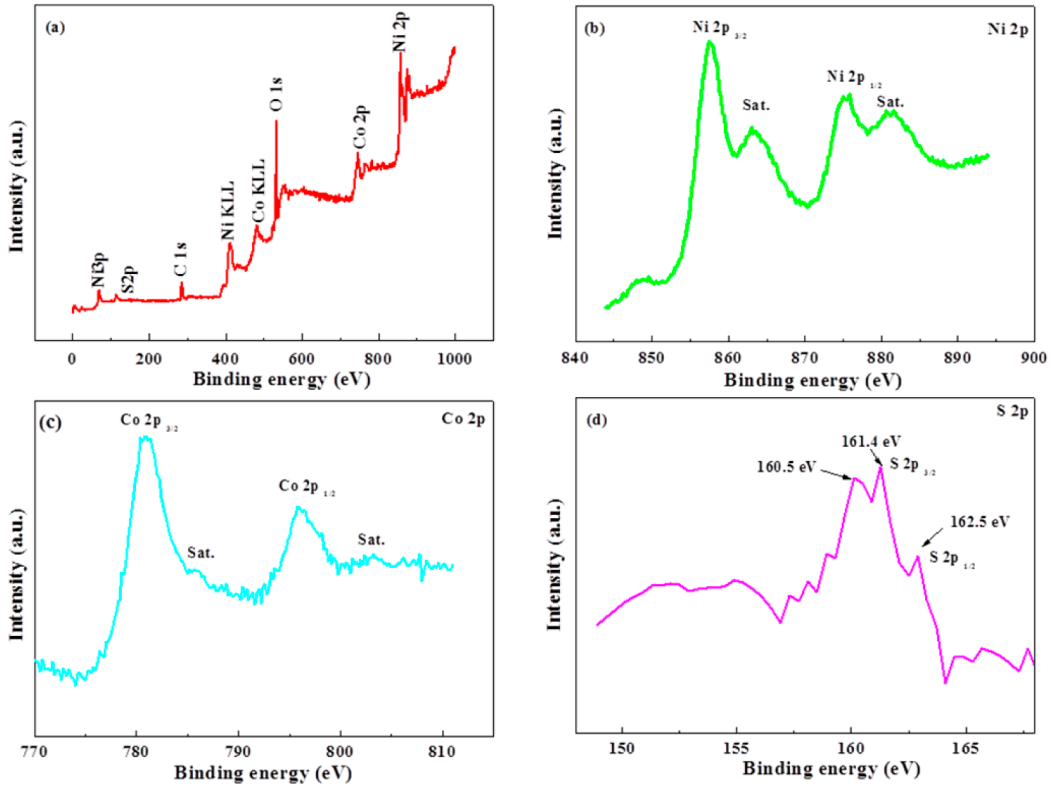

Figure 3. XPS spectra of CRNS-180 composite (a) the survey spectrum, (b) the Ni 2p spectrum, (c) the Co 2p spectrum, and (d) the S 2p spectrum.

indicates that, due to small size, CRNS has a large number of edges which act as defects and result in the raising of D peak.[26,30] Obviously, RGO in Co_9S_8/RGO/Ni_3S_2 composites has a deep reduction extent and a high level disorder.[26,31]

To further identify the chemical compositions of the CRNS-180 composite, XPS was performed. Figure 3a shows a survey XPS spectrum of the CRNS-180 sample. The peaks at 780.2 and 856.1 eV refer to Co 2p, and Ni 2p, respectively, while 1614 eV refers to S 2p, implying the presence of Ni, Co, and S elements in CRNS-180.[3] The elements of C and O are observed because of the existence of RGO. As depicted in Figure 3b, two main peaks at 874.4 and 856.6 eV in the Ni 2p XPS spectrum are assigned to Ni $2p_{1/2}$ and Ni $2p_{3/2}$, respectively, accompanied by the satellite peaks (referred as "sate.") and the energy difference between Ni $2p_{3/2}$ (856.6 eV) and Ni $2p_{1/2}$ (874.4 eV) is 17.8 eV, suggesting the coexistence of Ni^{2+} and Ni^{3+}.[6,32] In Figure 3c, the intensive peaks at 780.5 eV (Co $2p_{3/2}$) and 796.7 eV (Co $2p_{1/2}$) are illustrated, suggesting the presence of both Co^{3+} and Co^{2+} in CRNS-180 sample.[6,33] Figure 3d exhibits the intensive peaks at 160.5 and 161.4 eV belonging to S $2p_{3/2}$, while the peak at 162.5 eV can be assigned to S $2p_{1/2}$.[3,6] These XPS results are quite consistent with the XRD analysis mentioned above.

Parts a–d of Figure 4 illustrate the FESEM images of CRNS composites synthesized at different temperatures, i.e., CRNS-150, -180, -210, and -240, respectively. For all of these composites, the surface of NF was fully covered by interconnected nanoflakes of Ni_3S_2 and Co_9S_8, which are similar to the morphology of RNS-180, as shown in our previous work.[19] It is clearly observed that the temperature mainly affects the nanoflakes size and depth of three-dimensional pore structure, which is constructed by the assembly of vertical nanoflakes with a thickness of several nanometers.

As for CRNS-180 (Figure 4b,f), it possesses an evenly distributed larger size of nanoflakes and forms highly open and relatively deep porous nanostructures, making optimal use of the grain surface readily accessible to liquid electrolyte and providing efficient channels for electron transport. We also provided two large-scale FESEM images of the Co_9S_8/RGO/Ni_3S_2 composite in Supporting Information Figure S3, which can present the overall structure including Ni foam template. These images combining with Figure 4b,f fully testify to the structural features of this Co_9S_8/RGO/Ni_3S_2 composite material. In addition, compared to CNS-180 with hierarchically spherical flower-like network structures (Figure 4e), this suggests that the presence of GO influenced the arrangement and structure size of Co_9S_8/Ni_3S_2 nanoflakes and facilitated the formation of open and porous conductive network structures of Co_9S_8/RGO/Ni_3S_2 composite films. Furthermore, the RGO sheets may be uniformly and efficiently dispersed on the Ni substrate surface, which provide a large surface area to anchor Ni_3S_2 and Co_9S_8 nanoparticles. This forms the special conjugated network nanostructure (Figure 4a–d), enhances effective ionic transfer between composite nanosheets and electrolytes, and then the interconnected Co_9S_8 and Ni_3S_2 nanoflake networks entirely cover the surface of RGO.[19,34,35] This conjecture will be later confirmed by the EDS and TEM images.

The structure of the CRNS-180 composite was further analyzed by using energy-dispersive X-ray spectroscopy (EDS) mappings. Parts a–f of Figure 5 show the elemental mapping of oxygen (Figure 5a), nickel (Figure 5b), cobalt (Figure 5c), sulfur (Figure 5d), and carbon (Figure 5e) of the composite for

DOI: 10.1021/am5088192
ACS Appl. Mater. Interfaces 2015, 7, 4861–4868

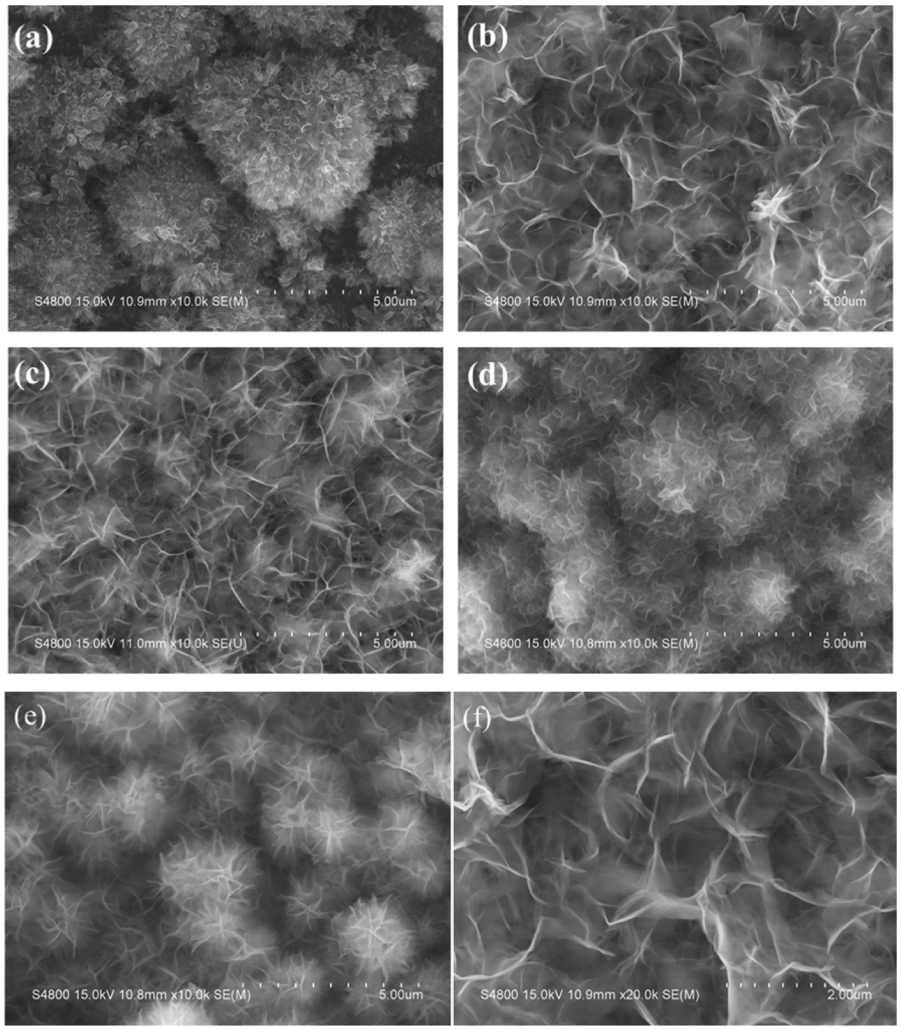

Figure 4. FESEM images of (a) CRNS-150 composite, (b) CRNS-180 composite, (c) CRNS-210 composite, (d) CRNS-240 composite, (e) CNS-180 composite, and (f) the enlarged view of (b).

the corresponding overlay image in Figure 5f. The even distribution of the elements including Ni, Co, and S elements confirms the uniform deposition of Co_9S_8/Ni_3S_2 nanoplates, which further confirms the successful preparation of the Co_9S_8/Ni_3S_2 nanoplates by this one-step hydrothermal method. The elemental maps convince that RGO is uniformly covered by the Co_9S_8/Ni_3S_2 nanoplates, which supports the SEM results.

Figure 6 shows the TEM and HRTEM images for CRNS-180 composite. As shown in Figure 6a, the interconnected nanoflakes are observed to be closely anchored on the RGO surface (different from those for Ni_3S_2/RGO).[19,34] The RGO support can also be seen underneath the nanoflakes. As seen in the magnification image (inset of Figure 6a), Co_9S_8/Ni_3S_2 nanoflakes are very thin and vertically insert RGO, leading to open and porous three-dimensional structures, which are beneficial to electrolyte access and electron transport during electrochemical reactions.[4,6,36] These results are in accordance with the SEM images.

The HRTEM image of CRNS-180 (Figure 6b) confirms that Co_9S_8 and Ni_3S_2 nanoflakes were well crystallized, with lattices of 0.244, 0.245, and 0.203 nm which are assigned to the *d*-spacing of the (331) planes, (400) planes of Co_9S_8, and the (202) planes of Ni_3S_2, respectively. The concentric rings of selected area electron diffraction (SAED) pattern given in the inset of Figure 6b confirms the polycrystallinity of the Co_9S_8 and Ni_3S_2 nanoflakes.[12,15]

3.2. Electrochemical Performances of Co_9S_8/RGO/Ni_3S_2 Composites. Figure 7a presents the cyclic voltammograms (CV) curves of $Co_9S_8/RGO/Ni_3S_2$ (CRNS) composite electrodes obtained at different temperatures (Figure 7a inset: the compared composites) with SR = 5 mV s^{-1}. A pair of redox peaks which is the indicator of pseudocapacitor, appear in the CV curves for all samples.[3,12] As shown in Figure 7a, area enveloped for the CRNS-180 composite is higher than those of composites prepared under other temperatures, suggesting higher specific capacitance. Additionally, it is observed that CRNS-180 exhibits much better performance than CNS-180 and RNS-180, which may be derived from the improved conductivity, fast electron transport, and the rapid ion diffusion of CRNS-180, originating from the spread of RGO coating and three-dimensional porous microstructure and the coupling of two metal species, offering a higher electronic conductivity and more redox reactions than the single component sulfides.[34,37]

Figure 7b presents the CV results of CRNS-180 measured at various scan rates. Obviously, the current response increased in the scan rate range of 2 to 20 mV s^{-1}. It is also apparent that a couple of redox peaks are seen in all CV curves. The redox peaks suggest that the capacitive ability is mainly resulted from

DOI: 10.1021/am5088192
ACS Appl. Mater. Interfaces 2015, 7, 4861−4868

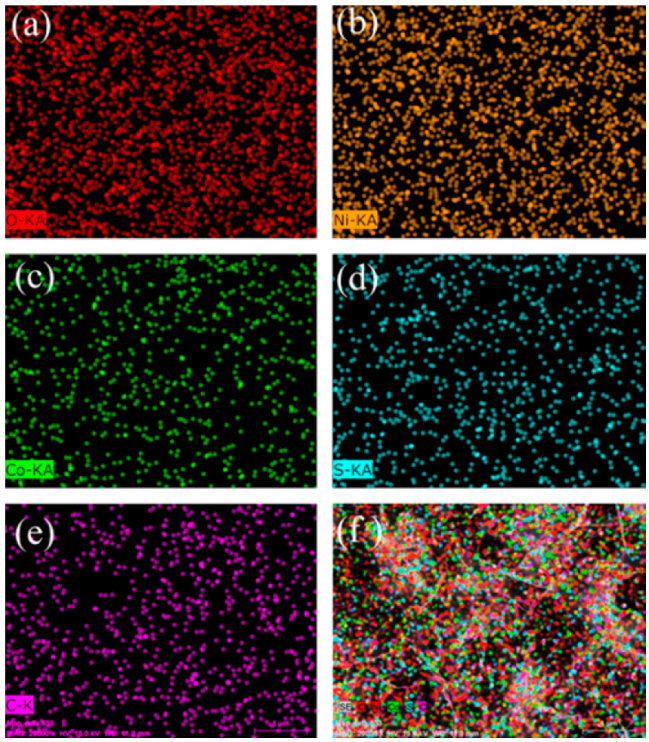

Figure 5. EDS mapping of the RNS32-180 composite of (a) O elements (red), (b) Ni elements (yellow), (c) Co elements (green), (d) S elements (blue), (e) C elements (purple), and (f) presents an overlay of O, Ni, Co, S, and C elements.

the Faradaic reaction related to M−S/M−S−OH, where M refers to Ni or Co. The reversible reactions in the alkaline electrolyte are suggested as follows.

$$Ni_3S_2 + 3OH^- \leftrightarrow Ni_3S_2(OH)_3 + 3e^- \quad (1)$$

$$Co_9S_8 + 9OH^- \leftrightarrow Co_9S_8(OH)_9 + 9e^- \quad (2)$$

With the scan rates, both the current density and the distance between the anodic and cathodic peaks increase, reflecting that the fast redox reactions occur at the interface of active material (solid)/electrolyte (solution).

The specific capacitance C_S (listed in Table 1) can be calculated as the following equation:[6]

$$C_S = \frac{C}{S} = \frac{I \times \Delta t}{\Delta V \times S} \quad (3)$$

where ΔV (V) is the potential window, I (A) is the charge−discharge current, Δt (s) is the discharge time, and S (cm^2) is the geometric surface area of CRNS composite electrodes.

Table 1 lists the capacitances at 20 mA cm^{-2} for all of the composites. It shows that the capacitance of CRNS increases with the hydrothermal temperature when the range increase from 150 to 180 °C and then decreases with further increasing from 180 to 240 °C. Consequently, CRNS-180 exhibits highest specific capacity (13.53 F cm^{-2}, 2611.9 F g^{-1}), which is much better than CNS-180 and RNS-180 composite electrodes.

Charge−discharge measurements were performed at various current densities of 20, 30, 40, 50, 60, 70, and 80 mA cm^{-2} (corresponding to 13.53, 12.29, 11.59, 10.73, 10.41, 10.03, and 9.40 F cm^{-2}, respectively) for CRNS-180 electrode, respectively. As shown in Figure 8a, the capacitance mainly results from pseudocapacitance, which is in accordance with the CV results. It is obvious that the contribution from NF substrate can be neglected, as shown in Supporting Information Figure S2b, compared with Figure 8a. When the current density increases from 3.9 to 15.6 A g^{-1}, 69.5% capacitance was retained (1814.7 F g^{-1} vs 2611.9 F g^{-1}), suggesting an good rate performance. To the best of our knowledge, this specific capacitance value is higher than those nickel sulfide or cobalt sulfide composites as supercapacitor electrodes.[12,13,19,20,27] This great enhancement in the specific capacitance is attributed not only to the synergistic effect deriving from the more active sites provided by RGO nanosheets and the quick electron transport of the highly interconnected nanoflakes but also to the well-defined open porous nanostructure formed on the conductive substrate, which allows easy access of electrolyte to all of the nanoflakes and, thus, facilitates charge transport and ion diffusion without any blocks of a binder.[5,19,34]

The CRNS-180 composite electrodes also exhibit good cyclability (Figure 8b), with a stable capacitance (retention 91.7%) after 1000 times of charging/discharging at 80 mA cm^{-2}, which is much better than the CNS-180 composite (~84.0% capacity retention) and RNS-180 composite (~85.9% capacity retention). Additionally, at the initial 700 cycles, for CRNS-180, the area capacitance decreases from 9.40 to 8.64 F cm^{-2}, corresponding to 91.9% of the initial capacitance. A relatively small capacitance decrease from 8.64 to 8.57 F cm^{-2} can be found for the next 300 cycles, in which only 0.8% loss of area capacitance is achieved, showing a relatively high cycling stability. The area capacitance increases for both CRNS-180 and CNS-180 at the initial 100 cycles, resulting from the electrode activation increasing the available active sites.[19,38]

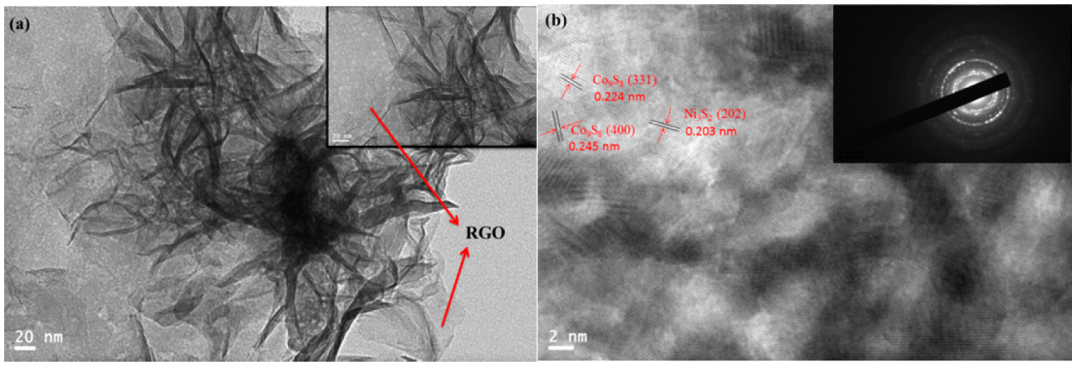

Figure 6. (a) TEM image of the CRNS-180 composite; inset, high magnification. (b) HR-TEM image of the CRNS-180 composite; inset, SAED pattern.

DOI: 10.1021/am5088192
ACS Appl. Mater. Interfaces 2015, 7, 4861−4868

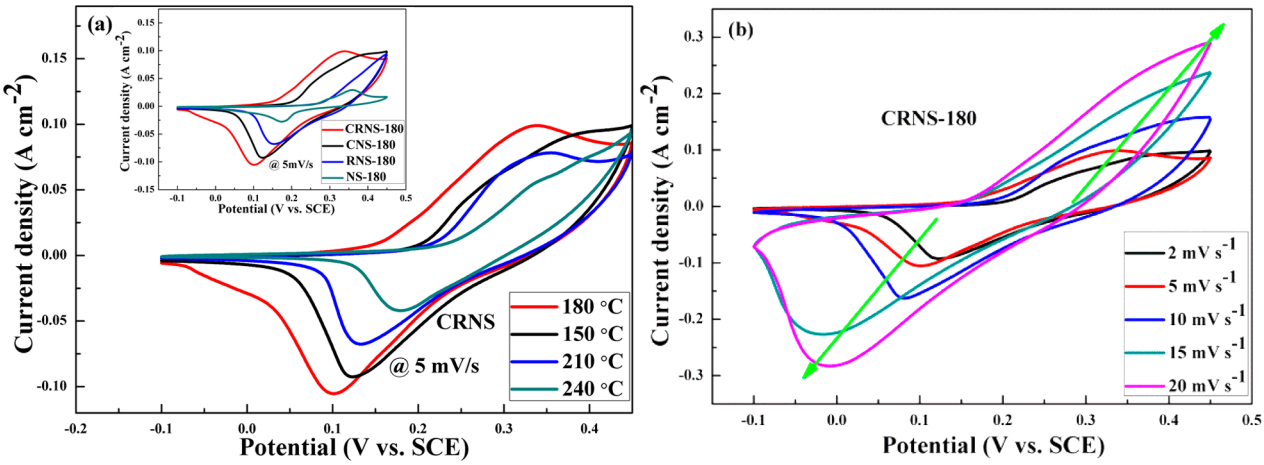

Figure 7. Cyclic voltammograms of (a) CRNS-150, 180, 210, and 240 at 5 mV s^{-1}; inset, cyclic voltammograms of contrast samples at 5 mV s^{-1}. (b) CRNS-180 electrode at various scan rates.

Table 1. Specific Capacitance for the Samples of Co_9S_8/RGO/Ni_3S_2-180, Co_9S_8/Ni_3S_2-180, and RGO/Ni_3S_2-180, Ni_3S_2-180, and Co_9S_8/RGO/Ni_3S_2-150, 210, and 240 at 20 mA cm^{-2}

samples	area capacitance (F cm^{-2})	mass capacitance (F g^{-1})
CRNS-150	11.78	2055.8
CRNS-180	13.53	2613.9
CRNS-210	10.31	1927.1
CRNS-240	3.72	941.8
CNS-180	7.02	1454.5
RNS-180	7.77	1726.7
NS-180	1.74	600

According to the electrochemical performance mentioned above, we can easily conclude that the Co_9S_8/RGO/Ni_3S_2 composite electrode is much better than bare Co_9S_8/Ni_3S_2 and RGO/Ni_3S_2 electrodes. The superior supercapacitive performance of the Co_9S_8/RGO/Ni_3S_2 composite may be based on the following features in structure. First, the RGO enhance the electron transport during charging/discharging process due to its high specific area and conductivity. Second, the highly open and deep 3D porous structure offers a short route and good accessibility for the solution.[19,34] The vertically connected nanoflakes supply a high specific surface area and many active sites, which can promote the pseudocapacitance at high rates.

Figure 9 illustrates the Nyquist plots of various composite electrodes recorded (100 kHz to 0.01 Hz). All the Nyquist

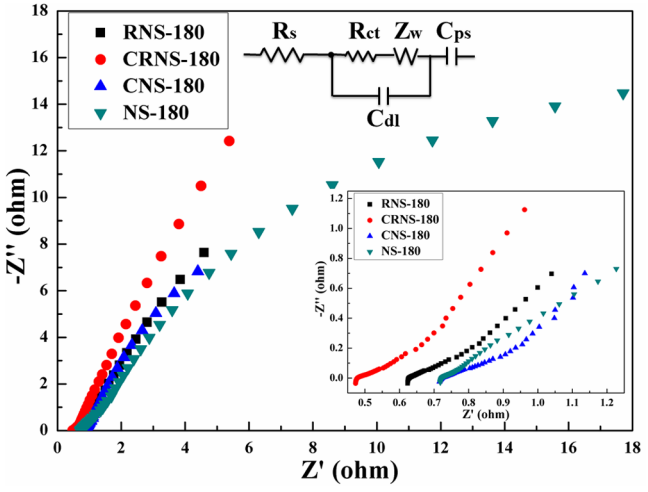

Figure 9. EIS of CRNS-180, CNS-180, RNS-180, and NS-180 composite electrodes in the frequency range from 100 kHz to 0.01 Hz. Inset: expanded views of the high frequency region displayed in the right part and the equivalent circuit diagram used for fitting impedance spectra in the upper part.

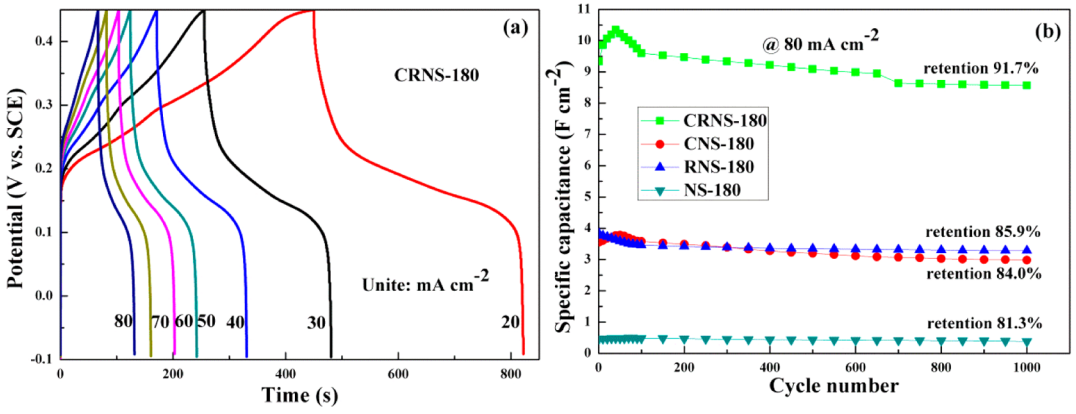

Figure 8. (a) Galvanostatic charge/discharge curves of CRNS-180 at various current densities. (b) Cycling performance of the CRNS-180, CNS-180, RNS-180, and NS-180 electrodes at a current density of 80 mA cm^{-2}.

DOI: 10.1021/am5088192
ACS Appl. Mater. Interfaces 2015, 7, 4861−4868

plots consist of a semicircle accompanied by a straight line at the low frequency region, which correspond to the electrochemical process and mass transfer process, respectively.[26,39] An equivalent circuit (inset of Figure 9) for fitting the EIS plots is composed of an equivalent series resistance (R_s), a charge-transfer resistance (R_{ct}), a double layer (C_{dl}) and a pseudocapacitive element (C_{ps}), and Warburg impedance (W). The X-intercept of the Nyquist plot at high frequency represents the equivalent series resistance (R_s) of the electrodes, whereas, the diameter of the semicircle corresponds to the resistance of charge transfer (R_{ct}) at the contact interface between the electrodes and electrolyte solution.[4,12] Obviously, the CRNS-180 has the smallest R_s value (0.47 Ω), and the R_{ct} values are smaller than 0.15 Ω, which is also lower than the CNS-180 (0.26 Ω), RNS-180 (0.20 Ω), and NS-180 (1.3 Ω). Additionally, the CRNS-180 composite electrode exhibits a line that is closer to vertical at the low frequency region, indicating that the CRNS-180 composite is a better candidate of electrode material for supercapacitors due to the low resistance of CRNS-180 and the contact resistance between Co_9S_8/RGO/Ni_3S_2 and substrate NF, which is supposed to raise the upper limit of the high charge−discharge rate of the supercapacitor. All of these results suggest that the CRNS-180 composite exhibits good rate capability, which is in accordance with the CV and GCD results.

4. CONCLUSIONS

We investigated a green, simple, one-step hydrothermal method for in situ growing of 3D petal-like network structures of Co_9S_8/RGO/Ni_3S_2 composite films on NF substrate and directly employed them as supercapacitor electrodes. This Co_9S_8/RGO/Ni_3S_2/NF electrode exhibits excellent capacitive performance (13.53 F cm^{-2} at 20 mA cm^{-2}, i.e., 2611.9 F g^{-1} at 3.9 A g^{-1}), compared with the Co_9S_8/Ni_3S_2/NF electrode (7.02 F cm^{-2}) and the RGO/Ni_3S_2/NF electrode (7.77 F cm^{-2}) prepared under identical conditions. Our work supplies a new strategy to directly (one-step) grow different RGO/metal sulfides composites of two kinds of metal sulfides with RGO on conductive metal substrates, which might have great potential in many fields.

■ ASSOCIATED CONTENT

Supporting Information

FESEM images of virgin NF and Co_9S_8/RGO/Ni_3S_2/NF composite after ultrasonic treatment; CV curves and chronopotentiometry of virgin NF and NF substrate after ultrasonic treatment to remove Co_9S_8/RGO/Ni_3S_2; FESEM images of the Co_9S_8/RGO/Ni_3S_2 composite at different magnifications. This material is available free of charge via the Internet at http://pubs.acs.org.

■ AUTHOR INFORMATION

Corresponding Author

*Phone: +86-21-6425 0838. Fax: +86-21-64250838. E-mail: chongjunzhao@ecust.edu.cn.

Notes

The authors declare no competing financial interest.

■ ACKNOWLEDGMENTS

Thanks are due to NSFC (20504026), the Shanghai Committee of Science and Technology (13ZR1411900), Shanghai Leading Academic Discipline Project and Key Laboratory Project (B502, 08DZ2230500).

■ REFERENCES

(1) Yu, Z.; Duong, B.; Abbitt, D.; Thomas, J. Highly Ordered MnO_2 Nanopillars for Enhanced Supercapacitor Performance. *Adv. Mater.* **2013**, *25*, 3302−3306.

(2) Yu, Z.; Li, C.; Abbitt, D.; Thomas, J. Flexible, Sandwich-like Ag-Nanowire/PEDOT:PSS-Nanopillar/MnO_2 High Performance Supercapacitors. *J. Mater. Chem. A* **2014**, *2*, 10923−10929.

(3) Wei, W.; Mi, L.; Gao, Y.; Zheng, Z.; Chen, W.; Guan, X. Partial Ion-Exchange of Nickel Sulfide-Derived Electrodes for High Performance Supercapacitors. *Chem. Mater.* **2014**, *26*, 3418−3426.

(4) Li, Y.; Cao, L.; Qiao, L.; Zhou, M.; Yang, Y.; Xiao, P.; Zhang, Y. Ni-Co Sulfide Nanowires on Nickel Foam with Ultrahigh Capacitance for Asymmetric Supercapacitors. *J. Mater. Chem. A* **2014**, *2*, 6540−6548.

(5) Liu, Y.; Zhang, J.; Wang, S.; Wang, K.; Chen, Z.; Xu, Q. Facilely Constructing 3D Porous $NiCo_2S_4$ Nanonetworks for High-Performance Supercapacitors. *New J. Chem.* **2014**, *38*, 4045−4048.

(6) Pu, J.; Cui, F.; Chu, S.; Wang, T.; Sheng, E.; Wang, Z. Preparation and Electrochemical Characterization of Hollow Hexagonal $NiCo_2S_4$ Nanoplates as Pseudocapacitor Materials. *ACS Sustainable Chem. Eng.* **2014**, *2*, 809−815.

(7) Peng, S.; Li, L.; Tan, H.; Cai, R.; Shi, W.; Li, C.; Mhaisalkar, S.; Srinivasan, M.; Ramakrishna, S.; Yan, Q. MS_2 (M = Co and Ni) Hollow Spheres with Tunable Interiors for High-Performance Supercapacitors and Photovoltaics. *Adv. Funct. Mater.* **2014**, *24*, 2155−2162.

(8) Han, S.; Kim, H.; Song, M.; Kim, J.; Ahn, H.; Lee, J. Nickel Sulfide Synthesized by Ball Milling as An Attractive Cathode Material for Rechargeable Lithium Batteries. *J. Alloys Compd.* **2003**, *351*, 273−278.

(9) Liu, Q.; Zhang, J. A General and Controllable Synthesis of Co_mS_n (Co_9S_8, Co_3S_4, and $Co_{1-x}S$) Hierarchical Microspheres with Homogeneous Phases. *CrystEngComm* **2013**, *15*, 5087−5092.

(10) Jayalakshmi, M.; Rao, M. Synthesis of Zinc Sulfide Nanoparticles by Thiourea Hydrolysis and Their Characterization for Electrochemical Capacitor Applications. *J. Power Sources* **2006**, *157*, 624−629.

(11) Chen, Q.; Li, H.; Cai, C.; Yang, S.; Huang, K.; Wei, X.; Zhong, J. In Situ Shape and Phase Transformation Synthesis of Co_3S_4 Nanosheet Arrays for High-Performance Electrochemical Supercapacitors. *RSC Adv.* **2013**, *3*, 22922−22926.

(12) Chou, S. W.; Lin, J. Y. Cathodic Deposition of Flaky Nickel Sulfide Nanostructure as an Electroactive Material for High-Performance Supercapacitors. *J. Electrochem. Soc.* **2013**, *160*, D178−D182.

(13) Rakhi, R.; Alhebshi, N.; Anjum, D.; Alshareef, H. Nanostructured Cobalt Sulfide-on-Fiber with Tunable Morphology as Electrodes for Asymmetric Hybrid Supercapacitors. *J. Mater. Chem. A* **2014**, *2*, 16190−16198.

(14) Jin, R.; Zhou, J.; Guan, Y.; Liu, H.; Chen, G. Mesocrystal Co_9S_8 Hollow Sphere Anodes for High Performance Lithium Ion Batteries. *J. Mater. Chem. A* **2014**, *2*, 13241−13244.

(15) Wang, Z.; Pan, L.; Hu, H.; Zhao, S. Co_9S_8 Nanotubes Synthesized on The Basis of Nanoscale Kirkendall Effect and Their Magnetic and Electrochemical Properties. *CrystEngComm* **2010**, *12*, 1899−1904.

(16) Zhang, B.; Ye, X.; Dai, W.; Hou, W.; Xie, Y. Biomolecule-Assisted Synthesis and Electrochemical Hydrogen Storage of Porous Spongelike Ni_3S_2 Nanostructures Grown Directly on Nickel Foils. *Chem.—Eur. J.* **2006**, *12*, 2337−2342.

(17) Park, C.; Giustino, F.; Spataru, C.; Cohen, M.; Louie, S. Angle-Resolved Photoemission Spectra of Graphene from First-Principles Calculations. *Nano Lett.* **2009**, *9*, 4234−4239.

(18) Stoller, M.; Park, S.; Zhu, Y.; An, J.; Ruoff, R. Graphene-Based Ultracapacitors. *Nano Lett.* **2008**, *8*, 3498−3502.

DOI: 10.1021/am5088192
ACS Appl. Mater. Interfaces 2015, 7, 4861−4868

(19) Zhang, Z.; Zhao, C.; Min, S.; Qian, X. A Facile One-Step Route to RGO/Ni_3S_2 for High-Performance Supercapacitors. *Electrochim. Acta* **2014**, *144*, 100−110.
(20) Ramachandran, R.; Saranya, M.; Santhosh, C.; Velmurugan, V.; Raghupathy, B.; Jeong, S.; Grace, A. Co_9S_8 Nanoflakes on Graphene (Co_9S_8/G) Nanocomposites for High Performance Supercapacitors. *RSC Adv.* **2014**, *4*, 21151−21162.
(21) Ma, L.; Shen, X.; Ji, Z.; Wang, S.; Zhou, H.; Zhu, G. Carbon Coated Nickel Sulfide/Reduced Graphene Oxide Nanocomposites: Facile Synthesis and Excellent Supercapacitor Performance. *Electrochim. Acta* **2014**, *146*, 525−532.
(22) Xiao, J.; Wan, L.; Yang, S.; Xiao, F.; Wang, S. Design Hierarchical Electrodes with Highly Conductive $NiCo_2S_4$ Nanotube Arrays Grown on Carbon Fiber Paper for High-Performance Pseudocapacitors. *Nano Lett.* **2014**, *14*, 831−838.
(23) Zhang, L.; Yu, J.; Mo, M.; Wu, L.; Li, Q.; Kwong, K. A General Solution-Phase Approach to Oriented Nanostructured Films of Metal Chalcogenides on Metal Foils: The Case of Nickel Sulfide. *J. Am. Chem. Soc.* **2004**, *126*, 8116−8117.
(24) Li, D.; Li, X.; Hou, X.; Sun, X.; Liu, B.; He, D. Building A Ni_3S_2 Nanotube Array and Investigating Its Application as An Electrode for Lithium Ion Batteries. *Chem. Commun.* **2014**, *50*, 9361−9364.
(25) Feng, N.; Hu, D.; Wang, P.; Sun, X.; Li, X.; He, D. Growth of Nanostructured Nickel Sulfide Films on Ni Foam as High-Performance Cathodes for Lithium Ion Batteries. *Phys. Chem. Chem. Phys.* **2013**, *15*, 9924−9930.
(26) Min, S.; Zhao, C.; Chen, G.; Qian, X. One-Pot Hydrothermal Synthesis of Reduced Graphene Oxide/$Ni(OH)_2$ Films on Nickel Foam for High Performance Supercapacitors. *Electrochim. Acta* **2014**, *115*, 155−164.
(27) Pu, J.; Wang, Z.; Wu, K.; Yu, N.; Sheng, E. Co_9S_8 Nanotube Arrays Supported on Nickel Foam for High-Performance Supercapacitors. *Phys. Chem. Chem. Phys.* **2014**, *16*, 785−791.
(28) Xu, Y.; Bai, H.; Lu, G.; Li, C.; Shi, G. Flexible Graphene Films via The Filtration of Water-Soluble Noncovalent Functionalized Graphene Sheets. *J. Am. Chem. Soc.* **2008**, *130*, 5856−5857.
(29) Yan, J.; Fan, Z.; Sun, W.; Ning, G.; Wei, T.; Zhang, Q.; Zhang, R.; Zhi, L.; Wei, F. Advanced Asymmetric Supercapacitors Based on $Ni(OH)_2$/Graphene and Porous Graphene Electrodes with High Energy Density. *Adv. Funct. Mater.* **2012**, *22*, 2632−2641.
(30) Zu, S.; Han, B. Aqueous Dispersion of Graphene Sheets Stabilized by Pluronic Copolymers: Formation of Supramolecular Hydrogel. *J. Phys. Chem. C* **2009**, *113*, 13651−13657.
(31) Pei, S.; Cheng, H. The Reduction of Graphene Oxide. *Carbon* **2012**, *50*, 3210−3228.
(32) Liu, Q.; Jin, J.; Zhang, J. $NiCo_2S_4$@Graphene as a Bifunctional Electrocatalyst for Oxygen Reduction and Evolution Reactions. *ACS Appl. Mater. Interfaces* **2013**, *5*, 5002−5008.
(33) Chen, H.; Jiang, J.; Zhang, L.; Wan, H.; Qi, T.; Xia, D. Highly Conductive $NiCo_2S_4$ Urchin-like Nanostructures for High-Rate Pseudocapacitors. *Nanoscale* **2013**, *5*, 8879−8883.
(34) Peng, S.; Li, L.; Li, C.; Tan, H.; Cai, R.; Yu, H.; Mhaisalkar, S.; Srinivasan, M.; Ramakrishna, S.; Yan, Q. In Situ Growth of $NiCo_2S_4$ Nanosheets on Graphene for High-Performance Supercapacitors. *Chem. Commun.* **2013**, *49*, 10178−10180.
(35) Pan, Q.; Xie, J.; Liu, S.; Cao, G.; Zhu, T.; Zhao, X. Facile One-Pot Synthesis of Ultrathin NiS Nanosheets Anchored on Graphene and the Improved Electrochemical Li-Storage Properties. *RSC Adv.* **2013**, *3*, 3899−3906.
(36) Wang, Q.; Gao, R.; Li, J. Porous, Self-Supported Ni_3S_2/Ni Nanoarchitectured Electrode Operating through Efficient Lithium-Driven Conversion Reactions. *Appl. Phys. Lett.* **2007**, *90*, 143107.
(37) Du, W.; Wang, Z.; Zhu, Z.; Hu, S.; Zhu, X.; Shi, Y.; Pang, H.; Qian, X. Facile Synthesis and Superior Electrochemical Performances of $CoNi_2S_4$/Graphene Nanocomposite Suitable for Supercapacitor Electrodes. *J. Mater. Chem. A* **2014**, *2*, 9613−9619.
(38) Wang, A.; Wang, H.; Zhang, S.; Mao, C.; Song, J.; Niu, H.; Jin, B.; Tian, Y. Controlled Synthesis of Nickel Sulfide/Graphene Oxide Nanocomposite for High-Performance Supercapacitor. *Appl. Surf. Sci.* **2013**, *282*, 704−708.
(39) Zhai, T.; Wang, F.; Yu, M.; Xie, S.; Liang, C.; Li, C.; Xiao, F.; Tang, R.; Wu, Q.; Lu, X.; Tong, Y. 3D MnO_2−Graphene Composites with Large Areal Capacitance for High-Performance Asymmetric Supercapacitors. *Nanoscale* **2013**, *5*, 6790−6796.

DOI: 10.1021/am5088192
ACS Appl. Mater. Interfaces 2015, 7, 4861−4868